European Journal of Mechanics / A Solids 96 (2022) 104706

Contents lists available at ScienceDirect

European Journal of Mechanics / A Solids

journal homepage: www.elsevier.com/locate/ejmsol

Beam formulation and FE framework for architected structures under finite deformations

Carlos Perez-Garcia, Josue Aranda-Ruiz, Ramon Zaera, Daniel Garcia-Gonzalez *

Department of Continuum Mechanics and Structural Analysis, Universidad Carlos III de Madrid, Avda. de la Universidad 30, 28911 Leganés, Madrid, Spain

ARTICLE INFO

Keywords:
Finite element method
Beam formulation
Architected materials
Metamaterials
Finite deformation
Additive manufacturing

ABSTRACT

The breakthrough in additive manufacturing (AM) techniques is opening new routes into the conceptualisation of novel architected materials. However, there are still important roadblocks impeding the full implementation of these technologies in different application fields such as soft robotics or bioengineering. One of the main bottlenecks is the difficulty to perform topological optimisation of the structures and their functional design. To help this endeavour, computational models are essential. Although 3D formulations provide the most reliable tools, these usually present very high computational costs. Beam models based on 1D formulations may overcome this limitation but they need to incorporate all the relevant mechanical features of the 3D problem. Here, we propose a mixed formulation for Timoshenko-type beams to consistently account for axial, shear and bending contributions under finite deformation theory. The framework is formulated on general bases and is suitable for most types of materials, allowing for the straightforward particularisation of the constitutive description. To prove validity of the model, we provide original experimental data on a 3D printed elastomeric material. We first validate the computational framework using a benchmark problem and compare the beam formulation predictions with numerical results from an equivalent 3D model. Then, we further validate the framework and illustrate its flexibility to predict the mechanical response of beam-based structures. To this end, we perform original experiments and numerical simulations on two types of relevant structures: a rhomboid lattice and a bi-stable beam structure. In both cases, the numerical results provide a very good agreement with the experiments by means of both quantitative and qualitative results. Overall, the proposed formulation provides a useful tool to help at designing new architected materials and metamaterial structures based on beam components. The framework presented may open new opportunities to guide AM techniques by feeding machine learning optimisation algorithms.

1. Introduction

Additive manufacturing (AM), also known as 3D printing, has gained a great interest among both research and industrial fields during the recent years (Hossain et al., 2020; Hossain and Liao, 2020). This technology is based on controlled deposition of material and has been in constant development leading to a wide range of different techniques. One interesting field that is attracting great attention, is the use of these techniques to manufacture flexible structures with complex geometries. In this regard, one may find different alternatives attending to the nature of the deposition and curing processes: material jetting, material extrusion and vat photopolymerisation (VPP) (Zhang et al., 2021; Gao et al., 2015; Wang and Chen, 2015).

Among the different geometrically complex structures, lattice-based metamaterials are one of the most interesting ones due to the possibility of customising their mechanical properties without the need of changing the material selection (Shishvan et al., 2022; Guo et al., 2020; Deshpande et al., 2001; Smith et al., 2013; Molavitabrizi et al., 2022). To this end, these are composed of a repeating pattern known as unit cell (UC) that defines the mechanical behaviour at the macroscopic scale. These materials are thus engineered composites designed at the microstructural level for a desired function. With an appropriate design, the metamaterial physical properties can be programmed to respond in a particular manner to a specific stimulus (Lucarini et al., 2022; Wan, 2022; Bastola and Hossain, 2021). Even though this groundbreaking technology is in constant development and some novel results have already been obtained, an optimal conceptualisation and design of such structures is still challenging.

The main roadblock impeding the full implementation of metamaterials or architected structures relates to their geometrical design.

* Corresponding author.
E-mail addresses: carperez@ing.uc3m.es (C. Perez-Garcia), jaranda@ing.uc3m.es (J. Aranda-Ruiz), ramon.zaera@ing.uc3m.es (R. Zaera), danigarc@ing.uc3m.es (D. Garcia-Gonzalez).

https://doi.org/10.1016/j.euromechsol.2022.104706
Received 28 March 2022; Received in revised form 23 May 2022; Accepted 6 June 2022
Available online 14 June 2022

The great advance in AM technologies allows for million combinations of mesostructural arrangements and the determination of the optimal solution is rarely obvious. Experimental methods for finding such a solution are not feasible, generating a strong need of efficient computational tools to help in this endeavour. Generally, high fidelity approaches mostly consist in FE models based on 3D elements. Although 3D models are the most used due to their accuracy, they present the main disadvantage of requiring a very high computational cost. This issue becomes a key impediment when complex geometries are needed. This creates a need for extremely high computational sources or the search for simplified and efficient computational alternatives. To fill this gap, 1D models postulate themselves as ideal candidates to significantly reduce the computational cost. To this end, these models use a lower number of degrees of freedom while preserving the most relevant characteristics of the structural and material response. Although some 1D models have been proposed in the literature to address this problem, most of them do not include important information such as cross-section stretching effects, the consideration of large strain and rotation theory or the incorporation of shear force effects (Sauer and Mergel, 2014; He et al., 2018; Nampally et al., 2019; Ishaquddin and Gopalakrishnan, 2021; Damanpack and Bodaghi, 2021; Mergel et al., 2014; Sauer and Wriggers, 2009; Doˇ gruoğlu and Kömürcü, 2019; Lepe et al., 2014). In addition to the above 2D formulations, some authors have developed three-dimensional approximations that allow more complex topologies to be simulated (Ortigosa et al., 2016; Liu et al., 2021; Yang et al., 2018; Choi et al., 2021; Borković et al., 2022; Huang et al., 2018; Levyakov, 2015). Furthermore, the implementation of the underlying mechanics of metamaterials in these frameworks is an interesting challenge to be achieved. This problem may be solved by developing new FE frameworks that make use of beam elements but maintain most of the relevant mechanical features.

In this work, we aim at providing an efficient FE framework to help at designing 3D-printed structures composed of latticed-based components. The formulation considers all important structural dependences while allowing for the implementation of further considerations without compromising its consistency. To this end, we developed a mixed FE formulation based on the Geometrically Exact Theory for Timoshenko-type beams to consistently account for axial, shear and bending contributions under finite deformation theory. The formulation has been developed in a two-dimensional coordinate system, given the large number of applications involving these type of lattice configurations (Damanpack et al., 2019; Bodaghi et al., 2017; Alkhader, 2020; Bluhm et al., 2020; Chen et al., 2019; Shan et al., 2015; Andrew et al., 2021; Wang et al., 2020). After particularisation of the constitutive equations defining appropriate hyperelastic energy potentials, the overall framework was validated against original experiments on AM beam-based structures considering lattice and bi-stable analyses. The complete framework presented has the potential to feed machine learning algorithms to optimise the design of architected structures. This may open new routes to conceptualise novel applications in soft robotics, bioengineering and actuator systems. Additionally, due to a generalised formulation, it may set the basis for metallic lattice structures manufacturing design (Schaedler et al., 2011).

2. Continuum mechanics formulation

A two-dimensional mixed finite element formulation based on the Geometrically Exact Theory for Timoshenko-type beam one-dimensional elements is used to consistently account for axial, shear and bending contributions under large strains theory (Wriggers, 2008). This point is essential when describing the mechanical behaviour of 3D-printed structures. In this regard, many novel applications are based on metamaterial structures where the cross-sectional plane loses the perpendicularity to the deformed axis. The local deformation of the cross-section is allowed, imposing the unique restriction of plane cross-section of the beam after deformations.

2.1. Kinematics

In a two-dimension Cartesian coordinate system, a straight beam of length L and rectangular cross-section with height H and width B is located coincident with the material X axis and the spatial x axis in the undeformed configuration Ω_0, see Fig. 1. In addition, a difference is made between a global spatial reference system $\mathbf{x} = \{x, y\}$ and a local spatial reference system $\hat{\mathbf{x}} = \{\hat{x}, \hat{y}\}$, which are related by the cross-section rotation θ in the deformed configuration Ω.

Let $\bar{\mathbf{u}} = \{\bar{u}, \bar{v}\}^T$ be the displacement vector of the centroid of the beam cross-section where $\bar{u}$ and $\bar{v}$ are the horizontal and the transverse displacements, respectively. In this regard, the displacement of a material point of the beam from its initial position $\mathbf{X}(X, Y)$ in the reference configuration Ω_0 to a new position $\mathbf{x}(x, y)$ in the current configuration Ω can be described by the centroid displacement vector $\bar{\mathbf{u}}$ as

$$\mathbf{u}(\mathbf{X}) = \begin{cases} u(X, Y, \theta) = \bar{u}(X) - Y \sin\theta(X) \\ v(X, Y, \theta) = \bar{v}(X) + Y \cos\theta(X) \\ \theta \end{cases}, \tag{1}$$

where u and v are the horizontal and transverse displacements of the material point.

The strain–displacement relations, derived using the principle of virtual work (Reissner, 1972), lead to

$$\boldsymbol{\epsilon} = \begin{Bmatrix} \lambda_c \\ \gamma \\ \kappa \end{Bmatrix} = \begin{Bmatrix} \left[1 + \bar{u}'\right] \cos\theta + \bar{v}' \sin\theta \\ \bar{v}' \cos\theta - \left[1 + \bar{u}'\right] \sin\theta \\ \theta' \end{Bmatrix}, \tag{2}$$

where $\boldsymbol{\epsilon} = \{\lambda_c, \gamma, \kappa\}^T$ is the strain vector with λ_c being the stretch of the centroid, γ the shear strain over the cross-section and κ the curvature of the axis passing through the centroid of the beam. Hereinafter, $(\,)'$ represents the derivative with respect to the coordinate X. The strain vector $\boldsymbol{\epsilon}$ in Eq. (2) can alternatively be written in its matrix form as

$$\boldsymbol{\epsilon} = \mathbf{R}(\theta)\, \mathbf{u}^*, \tag{3}$$

where the matrix $\mathbf{R}$ corresponds to the rotation matrix from global to local coordinate system defined as

$$\mathbf{R}(\theta) = \begin{bmatrix} \cos\theta & \sin\theta & 0 \\ -\sin\theta & \cos\theta & 0 \\ 0 & 0 & 1 \end{bmatrix}, \tag{4}$$

whereas $\mathbf{u}^*$ is a vector where the first two terms correspond to the first column of the deformation gradient $\mathbf{F}$ and the third one corresponds to the derivative of the cross-section rotation θ' giving

$$\mathbf{u}^* = \begin{Bmatrix} 1 + u' \\ v' \\ \theta' \end{Bmatrix}. \tag{5}$$

To define accurately the behaviour of beam-based structures, it is important to describe the cross-section variation due to longitudinal stretching effects. To this end, the current cross-section height h and width b are updated as

$$h = \int_{-H/2}^{H/2} \lambda_y(Y)\; dY, \qquad b = \frac{B}{H} \int_{-H/2}^{H/2} \lambda_z(Y)\; dY, \tag{6}$$

where λ_y and λ_z are the stretches in height and width directions, respectively. The method devised for the calculation of the stretches λ_y and λ_z is further detailed in Section 2.3. In these equations, two different considerations are taken into account. First, cross-section height h and width b are evaluated along the Y axis that passes through the centroid of the beam. Secondly, the stretch in width direction λ_z is defined as a function of coordinate Y considering the incompressibility condition $\lambda_z = \left(\lambda_x\ \lambda_y\right)^{-1}$. Note that axial stretch λ_x is function of the curvature κ and the coordinate y as $\lambda_x = \lambda_c + \kappa y$.

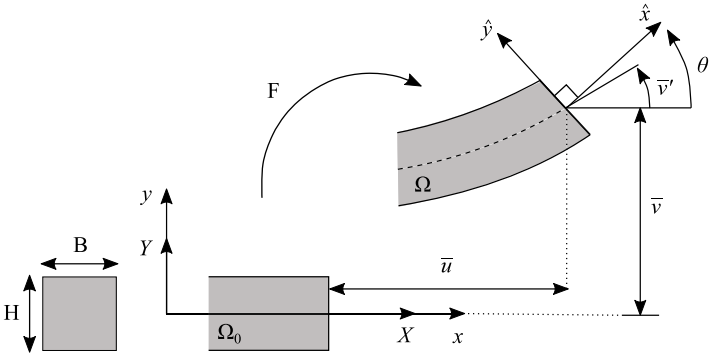

Fig. 1. Timoshenko beam-type nonlinear kinematics.

For the sake of convenience, we have considered a straight beam aligned with the X axis. In case the beam had an initial rotation Θ, this must be added to the current cross-section rotation θ. Consequently, the rotation matrix $\mathbf{R}$ must be reformulated as

$$\mathbf{R}(\Theta+\theta)=\begin{bmatrix}\cos(\Theta+\theta) & \sin(\Theta+\theta) & 0\\ -\sin(\Theta+\theta) & \cos(\Theta+\theta) & 0\\ 0 & 0 & 1\end{bmatrix}. \tag{7}$$

The previous expression is a particularisation of the general 3D multiplicative composition of rotation matrices, which is valid in this case since both rotation axes are coincident.

2.2. Weak formulation

The weak form of the equilibrium is based on the principle of virtual work as

$$\delta\Pi=\delta\Pi_{int}-\delta\Pi_{ext}=0, \tag{8}$$

where Π is the total potential energy while Π_{int} and Π_{ext} are the contributions of internal and external forces defined, respectively, as

$$\delta\Pi_{int}=\int_0^l \left[N\ \delta\lambda_c+Q\ \delta\gamma+M\ \delta\kappa\right]dx, \tag{9}$$

$$\delta\Pi_{ext}=\int_0^l \left[n\ \delta\bar{u}+q\ \delta\bar{v}+m\ \delta\theta\right]dx, \tag{10}$$

N being the axial force, Q the shear force and M the bending moment, the three of them contained in the stress resultant vector $\mathbf{S_r}=\{N,Q,M\}^T$. Moreover, n, q and m are the axial and perpendicular external loads and moment per unit length contained in the external load vector $\mathbf{q}=\{n,q,m\}^T$. Both Eqs. (9) and (10) are integrated along the beam length l in the current configuration Ω.

Substituting Eqs. (9) and (10) into Eq. (8), the weak form can be rewritten in its compact form as

$$\delta\Pi=\int_0^l \delta\boldsymbol{\varepsilon}^T\,\mathbf{S_r}\,dx-\int_0^l \delta\boldsymbol{\eta}^T\,\mathbf{q}\,dx=0, \tag{11}$$

where $\delta\boldsymbol{\eta}=\{\delta\bar{u},\delta\bar{v},\delta\theta\}^T$ are the virtual displacements of the centroid of the beam and the virtual rotation of the cross-section, respectively. The variation $\delta\boldsymbol{\varepsilon}$ of the strain measures shown in Eq. (2) for the geometrically exact model can be expressed as

$$\delta\boldsymbol{\varepsilon}=\mathbf{R}(\theta)\ \delta\boldsymbol{\eta}'+\frac{\partial\mathbf{R}(\theta)}{\partial\theta}\,\mathbf{u}^*\,\delta\theta. \tag{12}$$

2.3. Constitutive equations

The formulation presented can be generally applied to beam-based structures made of any kind of material. Among them, flexible materials that can undergo large deformations are of particular interest. This formulation is also suitable for these materials due to the consideration of finite deformation theory. To particularise the constitutive description, we have chosen hyperelastic energy potentials for reproducing 3D printed lattice structures subjected to large deformations.

Polymeric printable materials are characterised by a non-linear stress–strain relation and large deformations. The stress–strain constitutive relationship is defined from a strain energy density function Ψ that is formulated on the deformation gradient $\mathbf{F}$ allowing to develop a general formulation.

The deformation gradient $\mathbf{F}$ considered for a Timoshenko beam in x–y plane is defined as

$$\mathbf{F}=\begin{bmatrix}\lambda_x & 0 & 0\\ \gamma & \lambda_y & 0\\ 0 & 0 & \lambda_z\end{bmatrix}, \tag{13}$$

where λ_x, λ_y and λ_z are the stretches and γ is the shear deformation component.

From the definition of this energy, the first Piola–Kirchhoff stress tensor $\mathbf{P}$ can be derived as

$$\mathbf{P}=\frac{\partial\Psi}{\partial\mathbf{F}}, \tag{14}$$

and the Cauchy stress tensor $\boldsymbol{\sigma}$ can be obtained by the relation

$$\boldsymbol{\sigma}=J_F^{-1}\mathbf{P}\mathbf{F}^T, \tag{15}$$

where J_F is the determinant of the deformation gradient $\mathbf{F}$.

If the hyperelastic material is assumed incompressible, the first Piola–Kirchhoff stress tensor must be rewritten as

$$\mathbf{P}=\frac{\partial\Psi}{\partial\mathbf{F}}-J_F p\mathbf{F}^{-T}, \tag{16}$$

where p is a Lagrangian multiplier that ensures the incompressibility condition. Note that the relation in Eq. (15) is still valid. The stretches λ_y and λ_z as well as the pressure p are calculated by solving the system of equations $\sigma_{yy}=0$, $\sigma_{zz}=0$ and $\det(\mathbf{F})=1$.

From the Cauchy stress tensor, the stress resultant vector $\mathbf{S_r}$ can be calculated, in the current configuration, as

$$\mathbf{S_r}=\begin{cases}N=\int_{-h/2}^{h/2}\sigma_{xx}(\hat{y})\ b\,d\hat{y}\\ Q=\int_{-h/2}^{h/2}\sigma_{xy}(\hat{y})\ b\,d\hat{y}\\ M=\int_{-h/2}^{h/2}\sigma_{xx}(\hat{y})\ \hat{y}\ b\,d\hat{y}\end{cases}, \tag{17}$$

where the components of $\mathbf{S_r}$ are integrated along $\hat{y}$-direction considering the current cross-section height h and width b.

Deriving the stress resultants $\mathbf{S_r}=\{N,Q,M\}^T$ with respect to the strain variables $\boldsymbol{\epsilon}=\{\lambda_c,\gamma,\kappa\}^T$, the stiffness matrix $\mathbf{D}$, which relates variation of the stress resultants with strain variation for the hyperelastic material, can be obtained as

$$\mathbf{D}=\frac{\partial\mathbf{S_r}}{\partial\boldsymbol{\epsilon}}. \tag{18}$$

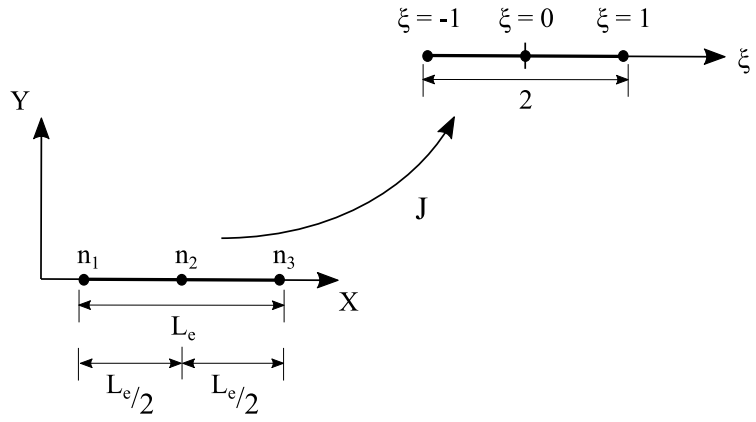

Fig. 2. Quadratic elements used in the Timoshenko beam-type nonlinear formulation.

3. Finite element framework

3.1. Spatial discretisation of the weak formulation

In this section, the weak formulation is discretised for its implementation in the finite element (FE) framework. Let us consider a two-dimensional spatial coordinate system $\mathbf{X} = \{X, Y\}$ and a natural coordinate system $\boldsymbol{\xi}$, see Fig. 2.

The element, with initial length L_e, is discretised into n_e quadratic finite beam elements with three nodes each ($n_{node} = 3$). Each node n_I, $I = 1, \dots, 3$, from the beam element has three degrees of freedom $\boldsymbol{u}_I = \{u_I, v_I, \theta_I\}^T$, corresponding to the horizontal and vertical displacements and the rotation of the beam element axis, respectively. Note that in the case of Fig. 2, the node n_2 is located equidistant to nodes n_1 and n_3.

The initial position of an element can be determined as

$$\mathbf{X^e} = \sum_{I=1}^{n_{node}} \mathbf{N}_I \, \mathbf{X}_I = \sum_{I=1}^{n_{node}} \mathbf{N}_I \begin{Bmatrix} X_I \\ Y_I \\ \theta_I \end{Bmatrix}, \tag{19}$$

and the element displacement as

$$\mathbf{u^e} = \sum_{I=1}^{n_{node}} \mathbf{N}_I \, \mathbf{u}_I = \sum_{I=1}^{n_{node}} \mathbf{N}_I \begin{Bmatrix} u_I \\ v_I \\ \theta_I \end{Bmatrix}, \tag{20}$$

where $\mathbf{N}_I$ is the interpolation matrix corresponding to node I

$$\mathbf{N}_I = \begin{bmatrix} N_I^u & 0 & 0 \\ 0 & N_I^v & 0 \\ 0 & 0 & N_I^\theta \end{bmatrix}. \tag{21}$$

For each element, with local node connectivities $\{1, 2, 3\}$ according to Fig. 2, quadratic shape functions are used to avoid locking issues (Damanpack and Bodaghi, 2021):

$$\begin{cases} N_1^n(\xi) = \frac{1}{2}[\xi - 1]\,\xi \\ N_2^n(\xi) = 1 - \xi^2 \\ N_3^n(\xi) = \frac{1}{2}[\xi + 1]\,\xi \end{cases}, \tag{22}$$

with $n = \{u, v, \theta\}$ being the active degree of freedom.

The beam element strain measures $\boldsymbol{\varepsilon}^e$ can be described as

$$\boldsymbol{\varepsilon}^e = \sum_{I=1}^{n_{node}} \mathbf{R}(\theta)\ \mathbf{B}_I\ \mathbf{u}_I^* = \sum_{I=1}^{n_{node}} \mathbf{R}(\theta)\ \mathbf{B}_I \begin{Bmatrix} 1 + u_I \\ v_I \\ \theta_I \end{Bmatrix}, \tag{23}$$

where $\mathbf{B}_I$ is the interpolation matrix which contains the partial derivative of the shape functions $\mathbf{N}_I$, giving

$$\mathbf{B}_I = \begin{bmatrix} \frac{\partial N_I^u}{\partial X} & 0 & 0 \\ 0 & \frac{\partial N_I^v}{\partial X} & 0 \\ 0 & 0 & \frac{\partial N_I^\theta}{\partial X} \end{bmatrix}, \tag{24}$$

that can be alternatively expressed as

$$\mathbf{B}_I = \frac{\partial \mathbf{N}_I}{\partial X} = \frac{\partial \mathbf{N}_I}{\partial \xi}\left[\frac{\partial X}{\partial \xi}\right]^{-1}, \tag{25}$$

where the determinant of the Jacobian matrix J can be computed as

$$J = \frac{\partial \xi}{\partial X} = \frac{L_e}{2}. \tag{26}$$

The displacement vector $\mathbf{u^e}$ obtained in Eq. (20) can be defined considering the rotation matrix $\mathbf{R}$ with respect to a local spatial reference system as

$$\hat{\mathbf{u}}^{\mathbf{e}} = \mathbf{R}(\theta)\,\mathbf{u}^{\mathbf{e}}. \tag{27}$$

Moreover, the strain vector $\boldsymbol{\varepsilon}^e$ is similarly defined following Eq. (3).

3.2. Internal and external forces

The internal forces are described throughout the definition of the internal virtual work. Considering the beam discretisation shown before, the variation of beam strain measures Eq. (12) is defined now as

$$\delta\boldsymbol{\varepsilon}^e = \sum_{I=1}^{n_{node}} \mathbf{B}_I^*\ \delta\boldsymbol{u}_I^* = \sum_{I=1}^{n_{node}} \mathbf{B}_I^* \begin{Bmatrix} \delta u_I \\ \delta v_I \\ \delta\theta_I \end{Bmatrix}, \tag{28}$$

where $\mathbf{B}_I^*$ is the interpolation matrix of strain variation of node I defined as

$$\mathbf{B}_I^* = \begin{bmatrix} \frac{\partial N_I^u}{\partial X}\cos\theta^e & \frac{\partial N_I^v}{\partial X}\sin\theta^e & \alpha_e\ N_I^\theta \\ -\frac{\partial N_I^u}{\partial X}\sin\theta^e & \frac{\partial N_I^v}{\partial X}\cos\theta^e & \beta_e\ N_I^\theta \\ 0 & 0 & \frac{\partial N_I^\theta}{\partial X} \end{bmatrix}, \tag{29}$$

with α_e and β_e as

$$\begin{cases} \alpha_e = -\left[1 + u^{e\prime}\right]\sin\theta^e + v^{e\prime}\cos\theta^e \\ \beta_e = -\left[1 + u^{e\prime}\right]\cos\theta^e + v^{e\prime}\sin\theta^e \end{cases}. \tag{30}$$

Note that the $\mathbf{B}_I^*$ matrix relates nodal degrees of freedom from vector $\boldsymbol{u}^e$ in global coordinates with the beam deformation in local coordinates.

Taking into account Eqs. (28) and (11), the internal forces $\mathbf{f}^{\mathbf{e}}_{\mathbf{int}}$ of the element can be defined as

$$\begin{aligned} \mathbf{f}^{\mathbf{e}}_{\mathbf{int}\,I} &= \int_{l_e} \mathbf{B}_i^*\ \mathbf{S}_{\mathbf{r}}\ dx \\ \mathbf{f}^{\mathbf{e}}_{\mathbf{int}} &= \sum_{I=1}^{n_{nodes}} \mathbf{f}^{\mathbf{e}}_{\mathbf{int}\,I} \end{aligned}, \tag{31}$$

that can be expressed in natural coordinates as

$$\mathbf{f}^{\mathbf{e}}_{\mathbf{int}\,I} = \int_{-1}^{1} \mathbf{B}_I^*(\xi)\ \mathbf{S}_{\mathbf{r}}(\xi)\ \frac{l_e}{2}\ d\xi, \tag{32}$$

where l_e is the current element length.

Regarding the external forces, these can be computed following a similar procedure reaching

$$\begin{aligned} \mathbf{f}^{\mathbf{e}}_{\mathbf{ext}\,I} &= \int_{l_e} \mathbf{N}_I\ \mathbf{q}\ dx \\ \mathbf{f}^{\mathbf{e}}_{\mathbf{ext}} &= \sum_{I=1}^{n_{nodes}} \mathbf{f}^{\mathbf{e}}_{\mathbf{ext}\,I} \end{aligned}. \tag{33}$$

Note that the previous summatories must be understood as an assembly process where the total internal and external forces vectors of the element are constructed from the nodal contributions.

3.3. Tangent stiffness matrix

The tangent stiffness matrix $\mathbf{K}^{\mathbf{e}}$ is obtained by the partial derivative of the associated internal and external force vectors with respect to the degrees of freedom as

$$\mathbf{K}^{\mathbf{e}}_{IJ} = \frac{\partial \left[\mathbf{f}^{\mathbf{e}}_{\mathbf{int}\,I} - \mathbf{f}^{\mathbf{e}}_{\mathbf{ext}\,I}\right]}{\partial \mathbf{u}^{\mathbf{e}}_J}. \tag{34}$$

The above expression can be further developed as

$$\begin{aligned} \mathbf{K}^{\mathbf{e}}_{IJ} &= \int_{l_e} \mathbf{B}_I^T \mathbf{D}\ \mathbf{B}_J\ dx + \int_{l_e} \left[N\ \mathbf{G}^{\mathbf{N}}_{IJ} + Q\ \mathbf{G}^{\mathbf{Q}}_{IJ}\right]\ dx \\ \mathbf{K}^{\mathbf{e}} &= \sum_{I=1}^{n_{nodes}} \sum_{J=1}^{n_{nodes}} \mathbf{K}^{\mathbf{e}}_{IJ} \end{aligned}, \tag{35}$$

where the first and second terms represent the material and geometrical components of $\mathbf{K}^{\mathbf{e}}$, respectively. As in Eqs. (31) and (33), the previous summatories must be understood as an assembly process. The matrices $\mathbf{G}^{\mathbf{N}}_{IJ}$ and $\mathbf{G}^{\mathbf{N}}_{IJ}$ are given by

$$\mathbf{G}^{\mathbf{N}}_{IJ} = \begin{bmatrix} 0 & 0 & -N_I^{u\prime}\ N_J^{\theta} \sin\theta^e \\ 0 & 0 & N_I^{v\prime}\ N_J^{\theta} \cos\theta^e \\ -N_I^{\theta}\ N_J^{u\prime} \sin\theta^e & N_I^{\theta}\ N_I^{v\prime} \cos\theta^e & \alpha_e^N\ N_I^{\theta}\ N_J^{\theta} \end{bmatrix}, \tag{36}$$

$$\mathbf{G}^{\mathbf{Q}}_{IJ} = \begin{bmatrix} 0 & 0 & -N_I^{u\prime}\ N_J^{\theta} \cos\theta^e \\ 0 & 0 & -N_I^{v\prime}\ N_J^{\theta} \sin\theta^e \\ -N_I^{\theta}\ N_J^{u\prime} \cos\theta^e & -N_I^{\theta}\ N_I^{v\prime} \sin\theta^e & \alpha_e^N\ N_I^{\theta}\ N_J^{\theta} \end{bmatrix}, \tag{37}$$

where

$$\begin{cases} \alpha_e^N = -\left[1 + u^{e\prime}\right] \cos\theta^e - v^{e\prime} \sin\theta^e \\ \alpha_e^Q = \left[1 + u^{e\prime}\right] \sin\theta^e - v^{e\prime} \cos\theta^e \end{cases}. \tag{38}$$

Note that the variational principle and the FE framework are formulated in the deformed configuration. Although one could easily adapt the formulation from one to each other, the spatial description allows for realistic force/moment boundary conditions in a straightforward manner. This feature is essential when implementing the numerical framework in some commercial FE software such as Abaqus.

4. Particularisation of constitutive equations

In this section, the constitutive equations presented in Section 2.3 are particularised for a specific hyperelastic constitutive model. The Lopez-Pamies model for rubber elastic materials is chosen since it accurately reproduces a wide range of deformation modes (Lopez-Pamies, 2010). The energy function reads as

$$\Psi = \sum_{k=1}^{n} \frac{3^{1-\alpha_k}}{2\alpha_k} G_k \left(I_{1,k}^{\alpha_k} - 3^{\alpha_k}\right), \tag{39}$$

where n is the model order, i.e., the number of constitutive terms, and $I_1 = tr\left(\mathbf{F}^{\mathbf{T}}\mathbf{F}\right)$. G_k and α_k are the material parameters. Note that $\sum_{k=1}^{n} G_k$ indicates the shear modulus of the material. The first Piola–Kirchhoff stress tensor, under incompressibility condition, can be derived as

$$\mathbf{P} = \frac{\partial \Psi}{\partial \mathbf{F}} - p\mathbf{F}^{-T} = \sum_{k=1}^{n} 3^{1-\alpha_k} G_k I_{1,k}^{\alpha_k - 1}\mathbf{F} - p\mathbf{F}^{-T}. \tag{40}$$

Taking into account the relation shown in Eq. (15), the Cauchy stress tensor can be calculated as

$$\boldsymbol{\sigma} = \sum_{k=1}^{n} 3^{1-\alpha_k} G_k \left(I_{1,k}^{\alpha_k - 1}\mathbf{F}\mathbf{F}^T\right) - p\ \mathbf{I}. \tag{41}$$

Considering the incompressibility condition, the deformation gradient $\mathbf{F}$ shown in Eq. (13) and free stress conditions in the transverse plane to the beam, the relevant Cauchy stress components are defined as

$$\sigma_{xx} = \sum_{k=1}^{n} \frac{-3^{1-\alpha_k}\ G_k \left(\gamma^2\ (\lambda_c + \kappa\ y) - 2\ (\lambda_c + \kappa\ y)^3 + \sqrt{4 + \gamma^4\ (\lambda_c + \kappa\ y)^2}\right) \left(\gamma^2 + (\lambda_c + \kappa\ y)^2 + \frac{\sqrt{(4+\gamma^4\ (\lambda_c+\kappa\ y)^2)}}{(\lambda_c+\kappa\ y)}\right)^{\alpha_k}}{2\ (\gamma^2\ (\lambda_c + \kappa\ y) + (\lambda_c + \kappa\ y)^3 + \sqrt{4 + \gamma^4\ (\lambda_c + \kappa\ y)^2})}, \tag{42}$$

$$\sigma_{xy} = \sum_{k=1}^{n} 3^{1-\alpha_k}\ G_k\ \gamma\ (\lambda_c + \kappa y) \left(\gamma^2 + (\lambda_c + \kappa\ y)^2 + \frac{\sqrt{4 + \gamma^4 (\lambda_c + \kappa y)^2}}{(\lambda_c + \kappa y)}\right)^{-1+\alpha_k}, \tag{43}$$

where σ_{xx} and σ_{xy} are the normal and tangential stresses acting on the beam cross-section.

The stress resultants $\mathbf{S}_{\mathbf{r}}$ in Eq. (17) are calculated using the Composite Simpson's 3/8 rule to integrate numerically the normal σ_{xx} and tangential σ_{xy} stress equations considering the current height h and width b of the beam cross-section. The constitutive matrix $\mathbf{D}$ is obtained applying central finite difference to derive stress resultants $\mathbf{S}_{\mathbf{r}}$ with respect to the strain vector $\boldsymbol{\varepsilon}$.

5. Material and experimental method

This section presents the material and methodology used to calibrate and validate the proposed computational framework. First, we introduce the material employed and the characterisation results to identify the constitutive parameters. Then, we motivate two beam-structures applications that serve to validate the model and show its applicability to the metamaterials field.

5.1. Material and constitutive calibration

One of the most promising applications of the model is its ability to predict the mechanical response of lattice-based structures manufactured by 3D printing technologies. The macrostructural behaviour of these structures can be modulated by designing specific arrangements

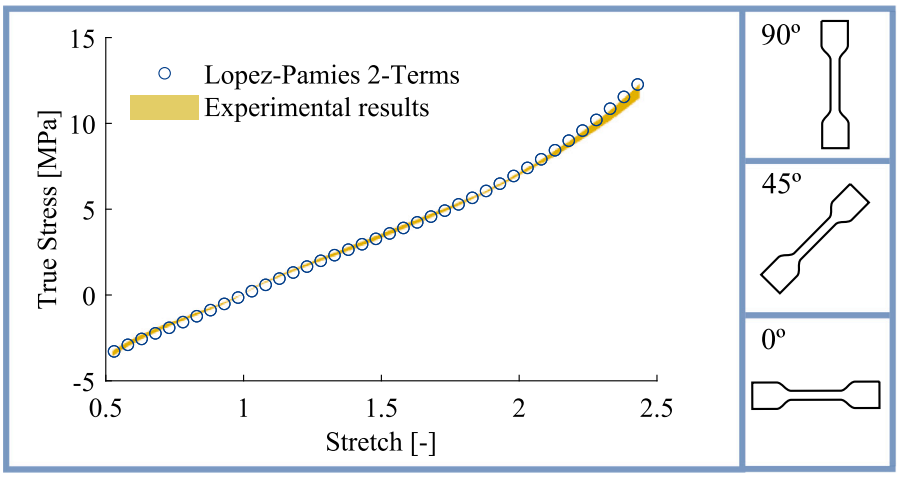

Fig. 3. Comparison between Lopez-Pamies hyper-elastic model prediction and experimental tensile and compression test results. The shaded region represents the results variability for different printing orientations.

of beam elements. In addition, these manufacturing techniques allow for using flexible polymeric materials that enable for undergoing large deformations. Among these, we chose a vat photo-polymerisation 3D printing technique known as Stereolithography (SLA). The material selected for the application is Flexible 80 A (Formlabs, Somerville, US). This material is provided in a resin form and cured via a point-by-point process using ultraviolet (UV) light having high level of accuracy with good finish and significant reduction of anisotropy.

To provide a first characterisation of the material to feed the constitutive model, we manufactured dog-bone shape specimens with dimensions according to the ASTM D638 standard for tensile characterisation and, cylindrical specimens with dimension according to the ISO 815-1:2019 standard for compression characterisation. These specimens are tested under quasi-static uniaxial tension using a displacement-controlled "Instron Series 3400" with a 50 N load cell, and with a testing speed equal to 10 mm/min. Six different samples are considered to evaluate anisotropy induced by the printing process. In this regard, three building orientations are selected: longitudinal (0°), oblique (45°) and transverse (90°), see Fig. 3. To ensure representativeness in experimental results, three specimens per printing orientation were tested giving a total of nine for tensile tests and nine for compression test. The experimental results of the stress–stretch curves for all these samples are shown in Fig. 3. No significant dispersion between samples conditions were observed, with all the samples presenting a mechanical response within the shaded region.

The tensile tests are used to calibrate the constitutive parameters of the Lopez-Pamies model. The non-linear response of this material requires the used of two constitutive branches, i.e., two terms in the model. The identification of these parameters is done by an optimisation algorithm that reduces the overall error between the model prediction and the experiment. After calibration, the identified parameters are $G_1 = 1.296$ MPa, $\alpha_1 = 1.611$, $G_2 = 1.182$ MPa and $\alpha_2 = -1.936$. A perfect agreement between model and experimental results is obtained, with the model prediction being within the experimental region along the whole stress–stretch curve, see Fig. 3. Note that the comparison is made in terms of Cauchy stress (true stress) versus stretch. Also note that the material tested can be modelled as isotropic with negligible effect of the printing orientation.

5.2. Experimental beam-based structures and testing conditions

To illustrate the flexibility and capabilities of the numerical framework, two different types of structures are considered: (A) a lattice-base structure, and (B) a bi-stable structure. Regarding the former, it consists in a rhomboid lattice geometrically defined by beams with initial length $L = 5$ mm, width $B = 3$ mm and aspect ratio $H/L = 0.12$ rotated initially $\Theta = \pm 50°$, see Fig. 4.A. This lattice is subjected to a quasi-static tensile test until reaching the breaking load which is close to deformations between 80% and 85%. To ensure optimal boundary conditions during the tests, we added handles parts on both the upper and lower sample region to attach to the grips (see Fig. 4.C).

Moreover, the second structure chosen corresponds to the unit cell proposed by Shan et al. (2015), which is specially interesting as it presents a bi-stability phenomenon. Such a response allows for the transition between equilibrium states triggered by a mechanical actuation. In addition, it adds difficulty to the numerical prediction of the problem compromising its convergence. The main geometrical features used in the manufacturing of the samples is presented in Fig. 4.B. Each unit cell is composed of two solid sections located at the upper and lower parts and two beams joining them. These beams have the same dimensions as those used in the rhomboid lattice. These samples are subjected to quasi-static compression loading, controlling the displacement of the upper solid part prior to the contact between the two solid parts occurs and obtaining different stable configurations. To ensure repeatability, three tests per condition were tested.

6. Numerical results

In this section, we first validate the computational framework by comparing the beam-based formulation (1D model) predictions with numerical results from an equivalent 3D model. Then, we present the experimental results for the lattice-based and the bi-stable structures, and use them to further validate the computational framework.

6.1. Validation of the computational framework

The computational framework is formulated on the basis of 1D elements that incorporates mechanical features of 3D beam-based structures. The first question arising is whether the model can faithfully reproduce the 3D characteristics of the problem, especially when the structure is subjected to important bending and shear components. To address this point, we consider a benchmark problem that is solved with our proposed formulation and a fully 3D FE model. The problem consists in a clamped-sliding beam that is subjected to a vertical displacement at the sliding end, as shown in Fig. 5. The initial dimensions of the beam are the same as those used in the samples tested experimentally. The simulations are run with the commercial software Abaqus using implicit integration. For both 1D and 3D models, we describe the beam material with the calibrated Lopez-Pamies model from the previous section.

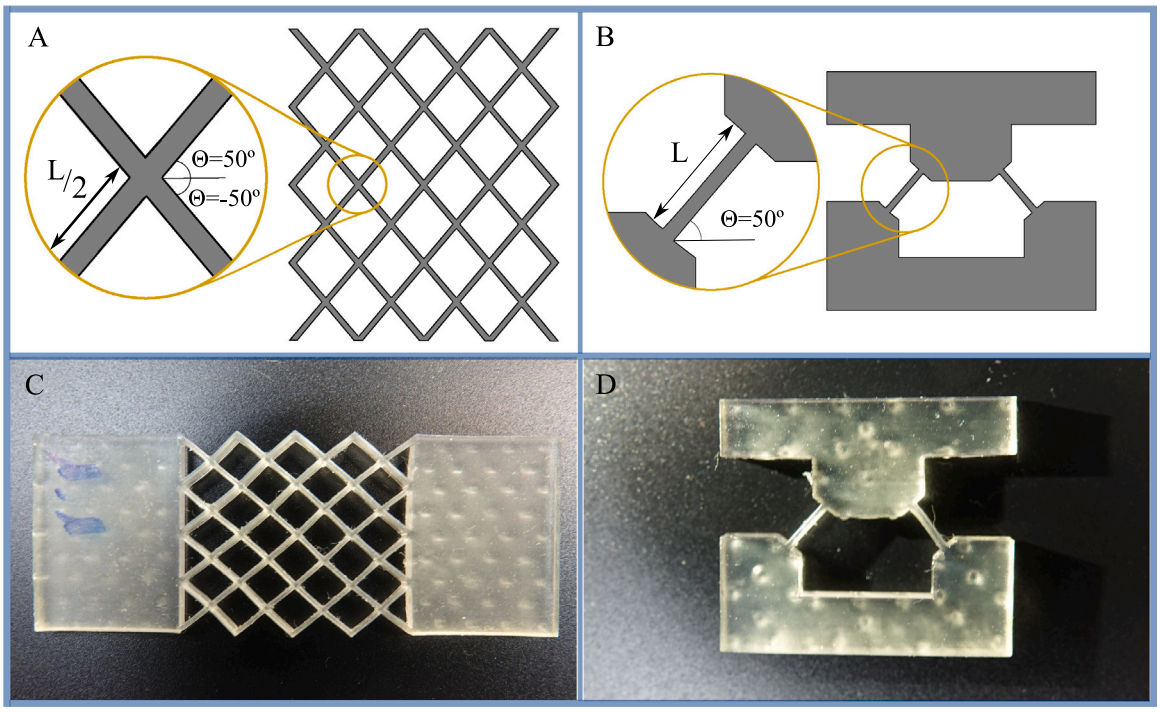

Fig. 4. Proposed experimental beam-based structures. Sub-panels (A) and (B) present the geometrical features of the unit cells used in the rhomboid and bi-stable lattices respectively. Sub-panels (C) and (D) show a representative 3D printed samples.

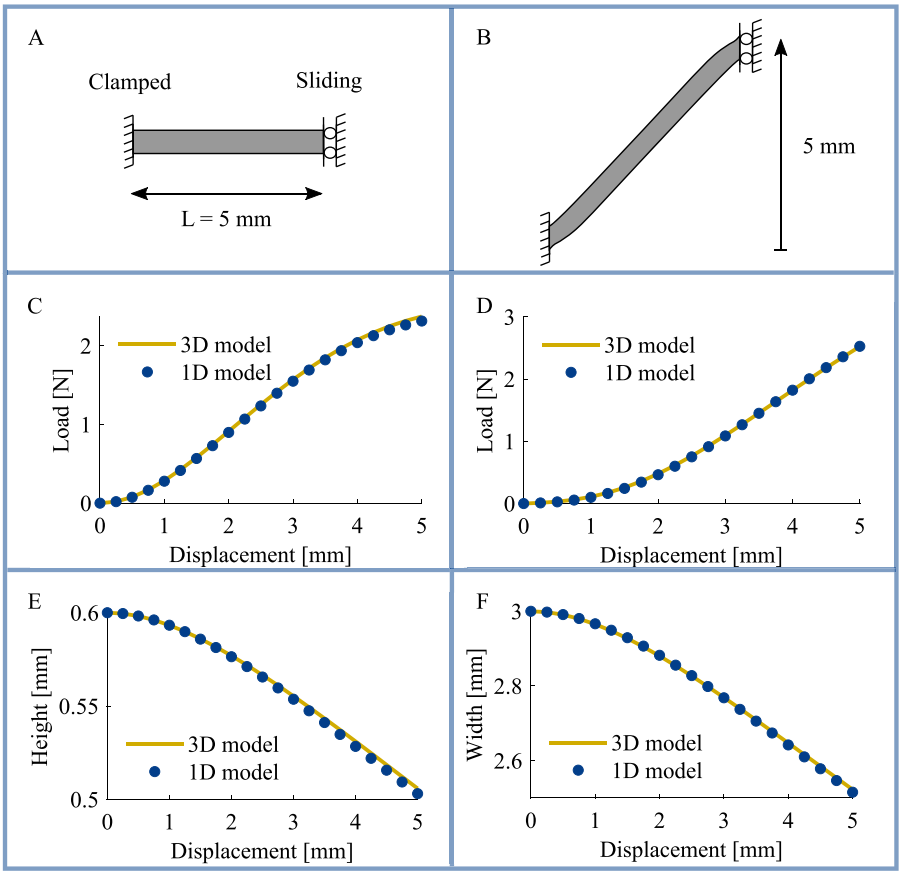

Fig. 5. Benchmark problem to validate the beam formulation against a 3D model: (A) Reference configuration, and (B) Deformed configuration. Comparison between the numerical results provided by the 1D and 3D models: (C) Horizontal reaction force versus vertical displacement; (D) Vertical reaction force versus vertical displacement; (E) Beam cross-section height variation of a beam section located at $L/2$; (F) Beam cross-section width variation of a beam section located at $L/2$.

For the 1D model, we implemented the whole FE framework in a UEL user-element subroutine, discretising the beam in three-nodes quadratic elements. Note that the material is assumed incompressible. Moreover, the 3D model consists of 20-node quadratic hybrid elements with linear pressure as additional degree of freedom to ensure incompressibility (C3D20H). The mechanical behaviour of the beam in the 3D case, i.e., Lopez-Pamies hyperelastic model, was defined using a UHYPER user-material subroutine. The comparison between the 1D and 3D models is shown in Fig. 5, in terms of vertical and horizontal reaction forces in the clamped region of the beam, as well as cross-sectional height and width versus vertical displacements. The agreement between both models is almost perfect, indicating a great reliability of the 1D formulation to simulate beam-based structures under large deformations.

6.2. Application to lattice and bi-stable structures

The previous results demonstrated the capability of the proposed formulation to model the mechanical response of a single beam-structure. Here, we further validate the computational framework modelling with more complex scenarios and comparing the numerical results with original experimental data. To this end, we first reproduce numerically the experiments conducted on the lattice-based structure. This problem allows for evaluating at once the reliability of the model to predict the mechanical response of local beam components as well as synergistic effects from the combined response of different beam-components. Then, we test the computational framework under even more complex mechanical conditions that introduce instability phenomena. To do so, we reproduce the experiments conducted on the bi-stable structure. Note that all these numerical simulations are compared with experiments using a flexible material so that important non-linear responses and large deformations are present.

The results for the rhomboid lattice structure are shown in Fig. 6.A and B. This figure provides a comparison between the 1D and 3D models prediction of the load evolution with displacement, with the experimental data (see Fig. 6.A). The numerical and experimental curves show a very good agreement. The fit between the experiment and the models is almost perfect in the first stages of deformation. A slightly higher discrepancy starts at very large deformations where the experimental force–displacement curve is almost linear, but the modelling predictions show a slight softening. This difference can be explained by the 3D printing manufacturing process that adds a higher stiffness in the beam-joints, see Dong and Zhao (2018). These joints are idealised in the numerical models and, consequently, the effective length reduction is not considered accurately. This issue becomes more relevant in the beam-formulation due to difficulties to represent the added joint stiffness. However, this discrepancy is almost negligible presenting a maximum error below 5%.

Moreover, a geometrical comparison of the sample deformation at different loading points is provided between the experiments and the proposed beam formulation (see Fig. 6.B). This figure also plots the stress distribution in the structure based on the beam-formulation results. The three different states chosen correspond to the initial configuration before deformation, a macroscopic strain of the whole structure equal to 50%, and a macroscopic strain close to the breaking load, i.e., 80%.

The deformed shape of the lattice obtained from the beam-formulation is superimposed to the experimental pictures corroborating an excellent agreement between experimental and modelling results. For each deformation state highlighted, a close look into a joint region, coincident with the maximum stresses reached, is included. These areas are located at the four corners of the lattice as a result of the maximum stretches reached in those beams and an important local bending contribution. Related to the numerical framework efficiency, the time required for the one-dimensional model was 20 times less than the three-dimensional model for the results shown in Fig. 6.A.

Note that other authors have considered similar rhomboid lattice geometry undergoing large deformations (see Damanpack et al. (2019)). In this work, however, an alternative manufacturing process (SLA) is used to obtain the structure using a resin with lower stiffness. These two facts allowed the authors reach higher stretch values close to twice the initial macroscopic lattice height and evaluate variations within the cross-section dimensions. In Fig. 7, the load evolution for a rhomboid lattice obtained with the 1D model considering and without considering cross-section variation is compared. The consideration of the cross-section variation leads to a response that presents a lower stiffness than without this consideration, what provides more reliable predictions when compared with experiments. This difference becomes more and more relevant at high strains.

The results for the bi-stable structure are shown in Fig. 6.C and D. Fig. 6.C compares the experimental and numerical results from both 1D and 3D models by means of force–displacement curve. As in the experimental test, displacement control has been imposed as boundary condition. In case of prescribing Neumann boundary conditions, the integration algorithm would require the use of arc-length methods to surpass the instability. The bi-stable transition in the experimental curve can be clearly observed by the null value reached in the force evolution, indicating a relative maximum in the energy evolution. This instability phenomenon is accurately captured by both the beam-formulation and the 3D model. Regarding this, all experimental and numerical curves reach the minimum force for the same displacement value. However, there is a higher difference between curves in the maximum force value and overall stiffness of the structure. The maximum displacements are close to 1 mm and show a worse agreement with the 1D model prediction. The first and most important source of discrepancy is the difficulty to experimentally keep the whole structure within the vertical plane, contrary to the numerical simulations that reproduce this in an ideal fashion. Due to the slenderness of the beams and without gluing the bottom and upper solid parts, any change in the alignment of the beam might result in slight out of plane movements which are corrected by the structured itself while it is compressed. However, this issue affects to the maximum and minimum experimental values. Still related to the boundary conditions, in the 1D model the end of the beam is fixed, whereas in the 3D model this boundary condition does not apply. Instead, the remaining geometry of the structure, i.e., non-beam region, is modelled as a deformable body. Similar to the previous analysis for the lattice structure, we compare experimental and numerical results by means of geometrical deformation, see Fig. 6.D. For this structure, we consider four relevant deformation states: (1) initial configuration, (2) deformation at reaching the maximum force, (3) deformation at reaching the minimum force, and (4) deformation prior to reaching contact between the beam and the supporting regions. The stress values are plotted in absolute value to show maximum stress concentration regions (note that for each beam section there are simultaneously tensile and compressive stresses due to bending). This problem is especially relevant for validation purposes as bending plays a very important role and, on top of that, the instability phenomenon associated to buckling can compromise the convergence of the numerical integration scheme. The importance of the bending contribution can be clearly observed by comparing the third and fourth states, where the maximum stress values are lower in the latter despite presenting higher stretching.

7. Conclusions

In this work, we propose a mixed formulation for Timoshenko-type beams, considering finite deformations, and its implementation within a robust computational framework that allows for predicting the mechanical response of architected structures. One of the novelties of the proposed work relies on a numerical framework for the beam-type elements that accounts for heterogeneous deformations within the cross-section, consistently with large strains theory and accounted for

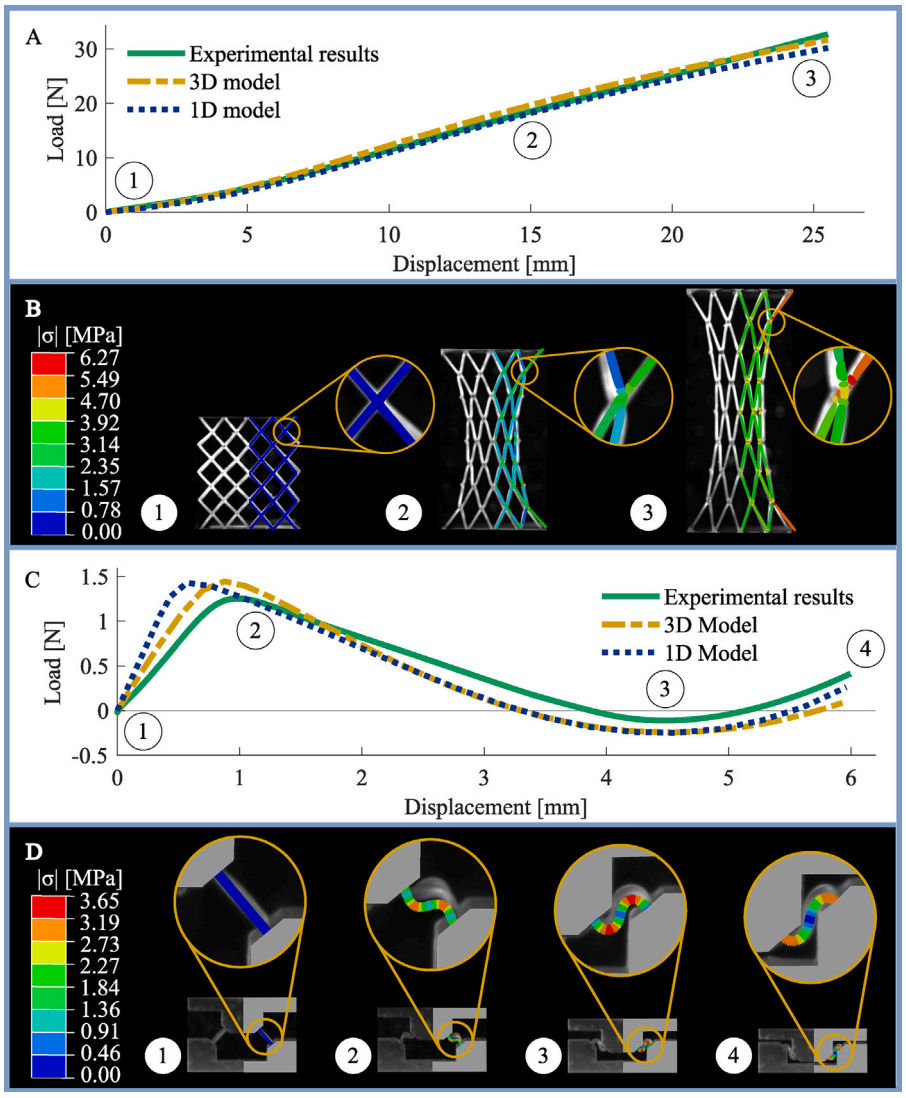

Fig. 6. Experimental and modelling results for the rhomboid structure: (A) Comparison of the experimental force–displacement curves with the 1D and 3D models predictions, and (B) geometrical deformation of the lattice, computed with the 1D model, at different deformation states indicated in sub-panel (A). These deformed shapes are overlapped with the corresponding experimental pictures, plotting the stress distribution within the lattice structure. Experimental and modelling results for the bi-stable structure: (C) Comparison of the experimental force–displacement curves with the 1D and 3D models predictions, and (D) geometrical deformation of the lattice, computed with the 1D model, at different deformation states indicated in sub-panel (C). These deformed shapes are overlapped with the corresponding experimental pictures, plotting the stress distribution within the lattice structure.

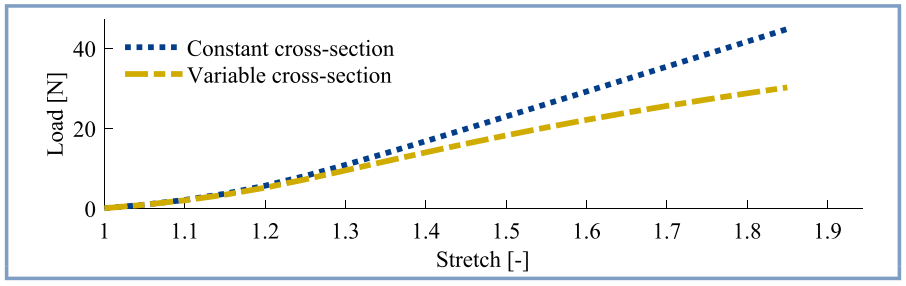

Fig. 7. Load versus stretch predictions using the beam-formulation when considering and without considering the heterogeneous variations along the cross-section for the rhomboid lattice structure.

axial, shear and bending contributions. This is done by considering the evolution of local stretches in height and width directions along the beam cross-section. This allows for a better description of normal and shear stress values within the cross-section and, consequently, more accurate stress resultant values. Furthermore, the complete framework is formulated on general bases allowing for the straightforward particularisation of the constitutive description, making it suitable for most types of materials. Contrary to other previous works, we formulate the whole framework in the deformed configuration. Although one could easily adapt the formulation from one to each other, the spatial

description allows for realistic force/moment boundary conditions in a straightforward manner. In addition, this description is especially interesting as many commercial software impose it.

To prove validity of the model we provide original experimental data on an elastomeric material manufactured using 3D printing by SLA with negligible anisotropic behaviour. After characterisation tests, the constitutive parameters are calibrated and the numerical framework is implemented in an implicit FE framework. The benchmark problem used to test reliability with respect to a 3D finite element model shows a perfect agreement with a considerable computational cost reduction. After that, we further validate experimentally the framework on two types of relevant complex beam-based structures: a rhomboid lattice and a bi-stable beam structure. In both cases, the numerical results provide a very good agreement with the experiments by means of both quantitative results, i.e., force–displacement curves, and qualitative results, i.e., geometrical deformation mechanisms. It should be noted the complexity of the problems tested that involve large deformations, important local bending and instability phenomena.

Overall, the proposed formulation provides an efficient solution to simulate the mechanical response of architected materials and metamaterial structures based on beam components. Along with the advanced additive manufacturing techniques available in the literature, it opens new opportunities to conceptualise novel functional structures. Promising avenues following this work are related to the use of multifunctional materials such as electro- (Soldner et al., 2021; Nasimsobhan et al., 2022; Mawassy et al., 2021; Chen et al., 2021) or magneto-active (Garcia-Gonzalez and Hossain, 2021; Moreno-Mateos et al., 2022; Yan et al., 2021; Sano et al., 2022) polymers. Another interesting application relies on the potential to couple the framework to machine learning algorithms for topological optimisation (Sun et al., 2022; Bastek et al., 2022), as well as its extension to three-dimensional problems.

CRediT authorship contribution statement

Carlos Perez-Garcia: Conceptualisation, Computational methodology, Experimental methodology, Investigation, Formal analysis, Writing – original draft, Writing – review & editing. **Josue Aranda-Ruiz:** Conceptualisation, Investigation, Experimental methodology, Writing – review & editing. **Ramon Zaera:** Conceptualisation, Computational methodology, Investigation, Formal analysis, Writing – review & editing. **Daniel Garcia-Gonzalez:** Conceptualisation, Computational methodology, Investigation, Formal analysis, Writing – original draft, Writing – review & editing.

Declaration of competing interest

The authors declare that they have no known competing financial interests or personal relationships that could have appeared to influence the work reported in this paper.

Acknowledgements

The authors acknowledge support from Ministerio de Ciencia e Innovacion MCIN/AEI/10.13039/501100011033 under Grant number PID2020-117894GA-I00, and the European Research Council (ERC) under the European Union's Horizon 2020 research and innovation programme (grant agreement No. 947723, project: 4D-BIOMAP). DGG acknowledges support from the Talent Attraction grant (CM 2018 - 2018-T2/IND-9992) from the Comunidad de Madrid. JAR acknowledges support from the Programa de Apoyo a la Realización de Proyectos Interdisciplinares de I + D para Jóvenes Investigadores de la Universidad Carlos III de Madrid and Comunidad de Madrid, Spain (project: OPTIMUM).

References

Alkhader, Maen, 2020. Localized strain fields in honeycomb materials with convex and concaved cells. Eur. J. Mech. 14.

Andrew, J. Jefferson, Alhashmi, Hasan, Schiffer, Andreas, Kumar, S., Deshpande, Vikram S., 2021. Energy absorption and self-sensing performance of 3D printed CF/PEEK cellular composites. Mater. Des. 208, 109863.

Bastek, Jan-Hendrik, Kumar, Siddhant, Telgen, Bastian, Glaesener, Raphal N., Kochmann, Dennis M., 2022. Inverting the structure–property map of truss metamaterials by deep learning. Proc. Natl. Acad. Sci. USA 119 (1), e2111505119.

Bastola, Anil K., Hossain, Mokarram, 2021. The shape – morphing performance of magnetoactive soft materials. Materials & Design (ISSN: 0264-1275) 211, 110172.

Bluhm, Gore Lukas, Sigmund, Ole, Wang, Fengwen, Poulios, Konstantinos, 2020. Nonlinear compressive stability of hyperelastic 2D lattices at finite volume fractions. J. Mech. Phys. Solids 137, 103851.

Bodaghi, M., Damanpack, A.R., Hu, G.F., Liao, W.H., 2017. Large deformations of soft metamaterials fabricated by 3D printing. Mater. Des. 131, 81–91.

Borković, A., Marussig, B., Radenković, G., 2022. Geometrically exact static isogeometric analysis of an arbitrarily curved spatial Bernoulli–Euler beam. Comput. Methods Appl. Mech. Engrg. 390, 114447.

Chen, Yangyang, Li, Xiaopeng, Scheibner, Colin, Vitelli, Vincenzo, Huang, Guoliang, 2021. Realization of active metamaterials with odd micropolar elasticity. Nature Commun. 12 (1), 5935.

Chen, Yiyao, Summers, Brock, Dahal, Ashutosh, Lauter, Valeria, Vignale, Giovanni, Singh, Deepak K., 2019. Field and current control of the electrical conductivity of an artificial 2D honeycomb lattice. Adv. Mater. 31 (16), 1808298.

Choi, Myung-Jin, Sauer, Roger A., Klinkel, Sven, 2021. An isogeometric finite element formulation for geometrically exact Timoshenko beams with extensible directors. Comput. Methods Appl. Mech. Engrg. 385, 113993.

Damanpack, A.R., Bodaghi, M., 2021. Large-deformation instability behaviors of 3D beams supported with 3D hinge joints subjected to axial and torsional loadings. Acta Mech. 232 (8), 2973–2989.

Damanpack, A.R., Bodaghi, M., Liao, W.H., 2019. Experimentally validated multi-scale modeling of 3D printed hyper-elastic lattices. Int. J. Non-Linear Mech. 108, 87–110.

Deshpande, V.S., Fleck, N.A., Ashby, M.F., 2001. Effective properties of the octet-truss lattice material. J. Mech. Phys. Solids 49 (8), 1747–1769.

Dong, Guoying, Zhao, Yaoyao Fiona, 2018. Numerical and experimental investigation of the joint stiffness in lattice structures fabricated by additive manufacturing. Int. J. Mech. Sci. 148, 475–485.

Gao, Wei, Zhang, Yunbo, Ramanujan, Devarajan, Ramani, Karthik, Chen, Yong, Williams, Christopher B., Wang, Charlie C.L., Shin, Yung C., Zhang, Song, Zavattieri, Pablo D., 2015. The status, challenges, and future of additive manufacturing in engineering. Comput. Aided Des. 69, 65–89.

Garcia-Gonzalez, Daniel, Hossain, Mokarram, 2021. Microstructural modelling of hard-magnetic soft materials: Dipole–dipole interactions versus Zeeman effect. Extreme Mechanics Letters 48, 101382.

Do˘ gruoğlu, Ali Nuri, Kömürcü, Sedat, 2019. Nonlinear mixed finite element formulations for the analysis of planar curved beams. Comput. Struct. 222, 63–81.

Guo, Honghu, Takezawa, Aikihiro, Honda, Masanori, Kawamura, Chikara, Kitamura, Mitsuru, 2020. Finite element simulation of the compressive response of additively manufactured lattice structures with large diameters. Comput. Mater. Sci. 175, 109610.

He, Liwen, Lou, Jia, Dong, Youheng, Kitipornchai, Sritawat, Yang, Jie, 2018. Variational modeling of plane-strain hyperelastic thin beams with thickness-stretching effect. Acta Mech 229 (12), 4845–4861.

Hossain, Mokarram, Liao, Zisheng, 2020. An additively manufactured silicone polymer: Thermo-viscoelastic experimental study and computational modelling. Addit. Manuf. 35, 101395.

Hossain, Mokarram, Navaratne, Rukshan, Perić, Djordje, 2020. 3D Printed elastomeric polyurethane: Viscoelastic experimental characterizations and constitutive modelling with nonlinear viscosity functions. Int. J. Non-Linear Mech. 126, 103546.

Huang, Chu Chang, Fujii, Fumio, Hsiao, Kuo Mo, 2018. An explicit algorithm for geometrically nonlinear transient analysis of spatial beams using a corotational total Lagrangian finite element formulation. Comput. Struct. 200, 68–85.

Ishaquddin, Md, Gopalakrishnan, S., 2021. Differential quadrature-based solution for non-classical Euler-Bernoulli beam theory. Eur. J. Mech. A Solids 86, 104135.

Lepe, Felipe, Mora, David, Rodríguez, Rodolfo, 2014. Locking-free finite element method for a bending moment formulation of Timoshenko beams. Comput. Math. Appl. 68 (3), 118–131.

Levyakov, S.V., 2015. Formulation of a geometrically nonlinear 3D beam finite element based on kinematic-group approach. Appl. Math. Model. 39 (20), 6207–6222.

Liu, Shuo, Fang, Guodong, Liang, Jun, Fu, Maoqing, Wang, Bing, Yan, Xiangqiao, 2021. Study of three-dimensional Euler-Bernoulli beam structures using element-based peridynamic model. Eur. J. Mech. A Solids 86, 104186.

Lopez-Pamies, Oscar, 2010. A new -based hyperelastic model for rubber elastic materials. Compt. Rendus Mécanique 338 (1), 3–11.

Lucarini, Sergio, Hossain, Mokarram, Garcia-Gonzalez, Daniel, 2022. Recent advances in hard-magnetic soft composites: Synthesis, characterisation, computational modelling, and applications. Compos. Struct. 279, 114800.

Mawassy, Nagham, Reda, Hilal, Ganghoffer, Jean-Francois, Eremeyev, Victor A., Lakiss, Hassan, 2021. A variational approach of homogenization of piezoelectric composites towards piezoelectric and flexoelectric effective media. Internat. J. Engrg. Sci. 158, 103410.

Mergel, Janine C., Sauer, Roger A., Saxena, Anupam, 2014. Computational optimization of adhesive microstructures based on a nonlinear beam formulation, 17.

Molavitabrizi, Danial, Ekberg, Anders, Mousavi, S. Mahmoud, 2022. Computational model for low cycle fatigue analysis of lattice materials: incorporating theory of critical distance with elastoplastic homogenization. European Journal of Mechanics - A/Solids (ISSN: 0997-7538) 92, 104480.

Moreno-Mateos, Miguel Angel, Gonzalez-Rico, Jorge, Nunez-Sardinha, Emanuel, Gomez-Cruz, Clara, Lopez-Donaire, Maria Luisa, Lucarini, Sergio, Arias, Angel, Muñoz Barrutia, Arrate, Velasco, Diego, Garcia-Gonzalez, Daniel, 2022. Magneto-mechanical system to reproduce and quantify complex strain patterns in biological materials. Appl. Mater. Today 27, 101437.

Nampally, Praneeth, Karttunen, Anssi T., Reddy, J.N., 2019. Nonlinear finite element analysis of lattice core sandwich beams. Eur. J. Mech. A Solids 74, 431–439.

Nasimsobhan, Maryam, Ganghoffer, Jean-François, Shamshirsaz, Mahnaz, 2022. Construction of piezoelectric and flexoelectric models of composites by asymptotic homogenization and application to laminates. Math. Mech. Solids 27 (4), 602–637.

Ortigosa, Rogelio, Gil, Antonio J., Bonet, Javier, Hesch, Christian, 2016. A computational framework for polyconvex large strain elasticity for geometrically exact beam theory. Comput. Mech. 57 (2), 277–303.

Reissner, Eric, 1972. On one-dimensional finite-strain beam theory: The plane problem. Z. Angew. Math. Phys. ZAMP 23 (5), 795–804.

Sano, Tomohiko G., Pezzulla, Matteo, Reis, Pedro M., 2022. A Kirchhoff-like theory for hard magnetic rods under geometrically nonlinear deformation in three dimensions. J. Mech. Phys. Solids 160, 104739.

Sauer, Roger A., Mergel, Janine C., 2014. A geometrically exact finite beam element formulation for thin film adhesion and debonding. Finite Elem. Anal. Des. 86, 120–135.

Sauer, Roger A., Wriggers, Peter, 2009. Formulation and analysis of a three-dimensional finite element implementation for adhesive contact at the nanoscale. Comput. Methods Appl. Mech. Engrg. 13.

Schaedler, T.A., Jacobsen, A.J., Torrents, A., Sorensen, A.E., Lian, J., Greer, J.R., Valdevit, L., Carter, W.B., 2011. Ultralight metallic microlattices. Science 334 (6058), 962–965, Publisher: American Association for the Advancement of Science.

Shan, Sicong, Kang, Sung H., Raney, Jordan R., Wang, Pai, Fang, Lichen, Candido, Francisco, Lewis, Jennifer A., Bertoldi, Katia, 2015. Multistable architected materials for trapping elastic strain energy. Adv. Mater. 27 (29), 4296–4301.

Shishvan, S.S., Dini Zarnagh, M.H., Deshpande, V.S., 2022. Energy dissipation and effective properties of a nominally elastic composite material. Eur. J. Mech. A Solids 92, 104452.

Smith, M., Guan, Z., Cantwell, W.J., 2013. Finite element modelling of the compressive response of lattice structures manufactured using the selective laser melting technique. Int. J. Mech. Sci. 67, 28–41.

Soldner, Dominic, Greiner, Sandra, Burkhardt, Christian, Drummer, Dietmar, Steinmann, Paul, Mergheim, Julia, 2021. Numerical and experimental investigation of the isothermal assumption in selective laser sintering of PA12. Addit. Manuf. 37, 101676.

Sun, Xiaohao, Yue, Liang, Yu, Luxia, Shao, Han, Peng, Xirui, Zhou, Kun, Demoly, Frédéric, Zhao, Ruike, Qi, H. Jerry, 2022. Machine learning-evolutionary algorithm enabled design for 4D-printed active composite structures. Adv Funct Materials 32 (10), 2109805.

Wan, Mengqi, 2022. 4D Printed programmable auxetic metamaterials with shape memory effects. Compos. Struct. 9.

Wang, Charlie, Chen, Yong, 2015. Geometric and physical modeling for additive manufacturing. Computer-Aided Design 69, 63–64.

Wang, Dong, Xu, Haipeng, Wang, Jinqiang, Jiang, Chengru, Zhu, Xiangyang, Ge, Qi, Gu, Guoying, 2020. Design of 3D printed programmable horseshoe lattice structures based on a phase-evolution model. ACS Appl. Mater. Interfaces 12 (19), 22146–22156, Publisher: American Chemical Society.

Wriggers, P., 2008. Nonlinear Finite Element Methods. Springer, Berlin, OCLC: ocn236120878.

Yan, Dong, Abbasi, Arefeh, Reis, Pedro M., 2021. A comprehensive framework for hard-magnetic beams: Reduced-order theory, 3D simulations, and experiments. Int. J. Solids Struct. 111319.

Yang, Xiao-Dong, Wang, Shao-Wen, Zhang, Wei, Yang, Tian-Zhi, Lim, C.W., 2018. Model formulation and modal analysis of a rotating elastic uniform Timoshenko beam with setting angle. Eur. J. Mech. A Solids 72, 209–222.

Zhang, Feng, Zhu, Liya, Li, Zongan, Wang, Shiyan, Shi, Jianping, Tang, Wenlai, Li, Na, Yang, Jiquan, 2021. The recent development of vat photopolymerization: A review. Addit. Manuf. 48, 102423.